Irreversible Organic Crystalline Chemistry Monitored in Real Time

Peter R. Poulin and Keith A. Nelson

Science **313**, 1756 (2006);
DOI: 10.1126/science.1127826

Science (print ISSN 0036-8075; online ISSN 1095-9203) is published weekly, except the last week in December, by the American Association for the Advancement of Science, 1200 New York Avenue NW, Washington, DC 20005.

molecules that persists into the postcleavage state (fig. S6).

Conclusion. The *glmS* ribozyme differs from typical riboswitches in two fundamental ways. First, the *glmS* ribozyme adopts a rigid fold that does not change upon metabolite binding (fig. S5) or during the course of the reaction (Fig. 3C). In contrast, conventional riboswitches couple the energy derived from metabolite binding to substantial conformational change of the RNA and only adopt a stable fold once they bind their cognate metabolites (*3*, *4*, *6*, *7*, *9*, *10*). Second, unlike the purine, S-adenosylmethionine, and thiamine pyrophosphate riboswitches, which achieve specificity by completely encapsulating their ligands (*3*, *4*, *7*, *9*, *10*), the *glmS* ribozyme achieves high specificity and satisfies its requirement for a precisely positioned functional group with a pK_a suitable for general acid-base catalysis using a solvent-accessible binding pocket. The open and rigid coenzyme-binding pocket of the *glmS* ribozyme, which is only partially filled by the natural ligand (Fig. 4B), appears to be an excellent target for the development of novel small-molecule activators or inhibitors that may have antibiotic properties.

References and Notes

1. W. C. Winkler, A. Nahvi, A. Roth, J. A. Collins, R. R. Breaker, *Nature* **428**, 281 (2004).
2. J. E. Barrick *et al.*, *Proc. Natl. Acad. Sci. U.S.A.* **101**, 6421 (2004).
3. R. T. Batey, S. D. Gilbert, R. K. Montange, *Nature* **432**, 411 (2004).
4. A. Serganov *et al.*, *Chem. Biol.* **11**, 1729 (2004).
5. T. E. Edwards, A. R. Ferré-D'Amaré, *Structure*, in press.
6. S. D. Gilbert, C. D. Stoddard, S. J. Wise, R. T. Batey, *J. Mol. Biol.* **359**, 754 (2006).
7. R. K. Montange, R. T. Batey, *Nature* **441**, 1172 (2006).
8. J. M. Carothers, J. H. Davis, J. J. Chou, J. W. Szostak, *RNA* **12**, 567 (2006).
9. A. Serganov, A. Polonskaia, A. T. Phan, R. R. Breaker, D. J. Patel, *Nature* **441**, 1167 (2006).
10. S. Thore, M. Leibundgut, N. Ban, *Science* **312**, 1208 (2006).
11. K. J. Hampel, M. M. Tinsley, *Biochemistry* **45**, 7861 (2006).
12. T. J. McCarthy *et al.*, *Chem. Biol.* **12**, 1221 (2005).
13. A. Roth, A. Nahvi, M. Lee, I. Jona, R. R. Breaker, *RNA* **12**, 607 (2006).
14. M. J. Fedor, J. R. Williamson, *Nat. Rev. Mol. Cell Biol.* **6**, 399 (2005).
15. A. T. Perrotta, I.-h. Shih, M. D. Been, *Science* **286**, 123 (1999).
16. S.-i. Nakano, D. M. Chadalavada, P. C. Bevilacqua, *Science* **287**, 1493 (2000).
17. S. R. Das, J. A. Piccirilli, *Nat. Chem. Biol.* **1**, 45 (2005).
18. P. B. Rupert, A. P. Massey, S. T. Sigurdsson, A. R. Ferré-D'Amaré, *Science* **298**, 1421 (2002); published online 10 October 2002 (10.1126/science.1076093).
19. J. A. Jansen, T. J. McCarthy, G. A. Soukup, J. K. Soukup, *Nat. Struct. Mol. Biol.* **13**, 517 (2006).
20. Y. Xue, Y. Xu, Y. Liu, Y. Ma, P. Zhou, *Int. J. Syst. Evol. Microbiol.* **51**, 1335 (2001).
21. Materials and methods are available as supporting material on *Science* Online.
22. S. R. Wilkinson, M. D. Been, *RNA* **11**, 1788 (2005).
23. C. W. A. Pleij, K. Rietveld, L. Bosch, *Nucleic Acids Res.* **13**, 1717 (1985).
24. M. H. Kolk *et al.*, *Science* **280**, 434 (1998).
25. P. Nissen, J. A. Ippolito, N. Ban, P. B. Moore, T. A. Steitz, *Proc. Natl. Acad. Sci. U.S.A.* **98**, 4899 (2001).
26. G. A. Soukup, *Nucleic Acids Res.* **34**, 968 (2006).
27. G. A. Soukup, R. R. Breaker, *RNA* **5**, 1308 (1999).
28. P. B. Rupert, A. R. Ferré-D'Amaré, *Nature* **410**, 780 (2001).
29. J. Salter, J. Krucinska, S. Alam, V. Grum-Tokars, J. E. Wedekind, *Biochemistry* **45**, 686 (2006).
30. T. M. Schmeing *et al.*, *Nat. Struct. Biol.* **9**, 225 (2002).
31. A. R. Ferré-D'Amaré, K. Zhou, J. A. Doudna, *Nature* **395**, 567 (1998).
32. T. S. Wadkins, A. T. Perrotta, A. R. Ferré-D'Amaré, J. A. Doudna, M. D. Been, *RNA* **5**, 720 (1999).
33. R. Pinard *et al.*, *EMBO J.* **20**, 6434 (2001).
34. L. L. Lebruska, I. I. Kuzmine, M. J. Fedor, *Chem. Biol.* **9**, 465 (2002).
35. P. C. Bevilacqua, *Biochemistry* **42**, 2259 (2003).
36. Y. I. Kuzmin, C. P. Da Costa, J. W. Cottrell, M. J. Fedor, *J. Mol. Biol.* **349**, 989 (2005).
37. H. B. White, *J. Mol. Evol.* **7**, 101 (1976).

38. We thank the staff at Advanced Light Source beamlines 5.0.1 and 5.0.2 and J. Bolduc for assistance with synchrotron and in-house x-ray data collection, respectively, and M. Been, R. Breaker, T. Edwards, T. Hamma, B. Kaiser, R. Klein, J. Pitt, J. Pizzarro, A. Roll-Mecak, B. Shen, J. Simon, G. Varani, and Y. Xiong for discussions. A.R.F. is a Distinguished Young Scholar in Medical Research of the W. M. Keck Foundation. D.J.K. is a Damon Runyon Fellow supported by the Damon Runyon Cancer Research Foundation (DRG-1863-05). This work was also supported by grants from the NIH (GM63576) and the W. M. Keck Foundation (both to A.R.F.). Atomic coordinates and experimental structure factor amplitudes for the 2′-amino and 2′-deoxy precleavage structures, the Glc6P-bound 2′-deoxy precleavage structure, and the postcleavage structure have been deposited with the Protein Data Bank under the accession codes 2GCS, 2H0S, 2H0Z, and 2GCV, respectively. The 2′-amino precleavage and the postcleavage structures obtained from crystals grown in the absence of GlcN6P have accession codes 2H0X and 2H0W, respectively. The structures obtained by soaking all-RNA crystals with Glc6P and GlcN6P have accession codes 2HO7 and 2HO6, respectively.

Supporting Online Material

www.sciencemag.org/cgi/content/full/313/5794/1752/DC1
Materials and Methods
SOM Text
Figs. S1 to S8
Tables S1 and S2
References

8 May 2006; accepted 17 July 2006
10.1126/science.1129666

REPORTS

Irreversible Organic Crystalline Chemistry Monitored in Real Time

Peter R. Poulin and Keith A. Nelson*

Because multiple laser shots are typically required to monitor ultrafast photochemical reaction dynamics, sample depletion and product accumulation have greatly restricted the range of substrates and structural environments amenable to study. By implementing a two-dimensional spatial delay gradient across the profile of a femtosecond probe pulse, we can monitor in a single laser shot organic crystalline reaction dynamics despite the formation of permanent photoproducts that cannot be conveniently removed. We monitored the photolysis of the triiodide anion, I_3^-, and subsequent recombination or relaxation of its reaction products, in three very different pure organic molecular crystals. The experimental results and associated molecular dynamics simulations illustrate the intimate connection between lattice structure and reaction dynamics, highlighting the role of lattice constraints in directing phase-coherent geminate recombination of photofragments within a crystalline reaction cage.

Direct time-resolved observation of chemistry in the solid state offers an experimental precision especially well suited to detailed modeling of local influences on reactivity. Advantages include the uniformity of the crystal lattice structure and the constraints it places on the motions of reactants and products; the limited number of well-defined lattice vibrational modes through which dynamical exchange of energy between the reacting species and the surroundings may occur; and the systematic variation of the lattice environment encountered in related members of a crystalline family (*1*–*4*). This potential for detailed analysis and understanding cannot be matched in liquid-state photochemistry, because even though short-time reaction dynamics in liquids also are strongly influenced by local intermolecular geometries and interactions, experimental measurements are invariably averaged over myriad local environments; consequently, the distinct time-dependent signatures of different surroundings are obscured. Mechanistic insight into the influence of crystal structure and local intermolecular topology on reaction dynamics and yields has been termed topochemistry (*1*) and discussed qualita-

Department of Chemistry, Massachusetts Institute of Technology, 77 Massachusetts Avenue, Cambridge, MA 02139, USA.

*To whom correspondence should be addressed. E-mail: kanelson@mit.edu

tively or semiquantitatively in terms of a reaction cage formed by the local lattice structure (*5*). Beyond its fundamental interest, such insight can guide the design of molecular crystals with applications ranging from solid-state organic synthesis to organic electronics to energetic materials. Direct time-resolved observation of ultrafast reaction dynamics in zeolites (*6*) and related porous structures would also be of considerable interest for catalyst optimization.

Unfortunately, the probing of ultrafast crystalline photochemistry using conventional techniques of femtosecond spectroscopy (*7*) is generally frustrated by the buildup of permanent reaction products and by the difficulty of replacing a degraded sample with fresh material, as achieved through flow in studies of liquid- or gas-phase samples. Thus, ultrafast spectroscopy of crystalline chemical reactions has been rare and has focused on a small set of reversible reactions in organic crystals and rare gas matrices (*8*). A generally applicable method for unrestricted study of photochemistry in complex organic lattice environments, including covalent bond breakage, molecular fragmentation into new chemical products, and product evolution, has been lacking. Here we apply a single-shot probing approach that reveals crystalline reaction dynamics with femtosecond resolution.

To gauge the impact of lattice environment on reactivity, we studied three pure molecular crystals, each containing the same photolabile anion, triiodide (I_3^-), and a different complex organic counterion (*9*). The substantial differences in lattice structure are evident from the crystal structures (Fig. 1) of tetra-*n*-butylammonium triiodide (TBAT) (*10*), tetraethylammonium triiodide (TEAT) (*11*), and tetraphenylphosphonium triiodide (TPPT), determined through x-ray diffraction.

Gas and liquid-state spectroscopy (*12*–*19*) have established that photoexcitation of I_3^- at an ultraviolet (UV) wavelength of 300 nm leads to rapid dissociation, yielding a bound I_2^- anion and a neutral I atom. The I_2^- species may be probed through its broad absorption band in the visible and near-infrared (IR) spectral regions without interference from the I_3^- UV absorption. In all three crystalline systems, exposure to a single weak UV excitation pulse (*9*) produces a clearly visible, permanent discoloration of the crystal at the site of irradiation. The usual approach to femtosecond spectroscopy of repeated sample excitation, with data accumulated over many thousands of laser shots, was clearly inapplicable to solution-grown crystals, each offering only a small region of acceptable optical quality for measurement.

To circumvent this problem, we developed a technique to acquire multiple time-resolved data points with a single laser pulse. The use of an echelon structure (Fig. 2B) to subdivide the transverse profile of a probe beam into multiple distinct pulses, each of which reaches the sample at a different time, was introduced in the early days of picosecond spectroscopy (*20*). However, the scheme was difficult to implement and was supplanted by the use of a variable delay line (Fig. 2A). The echelon

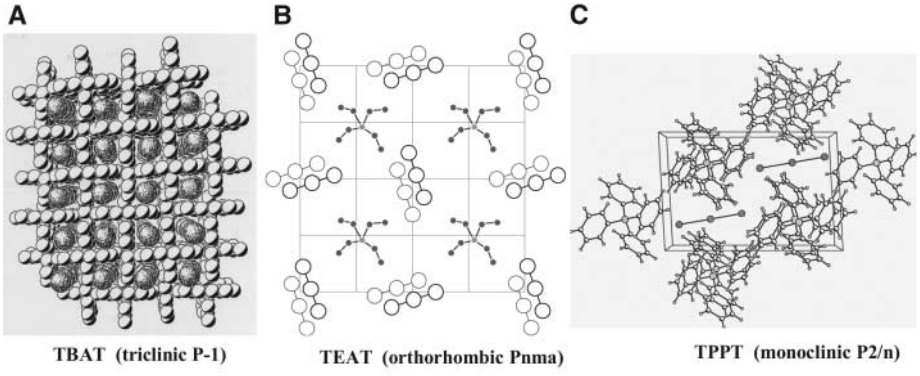

Fig. 1. Crystal structures of (**A**) tetra-*n*-butylammonium triiodide (TBAT), (**B**) tetraethylammonium triiodide (TEAT), and (**C**) tetraphenylphosphonium triiodide (TPPT). The structures are determined by x-ray diffraction. I_3^- ions are oriented in approximately longitudinal columnar chains in TBAT and in nearly orthogonal side-on stacks in TEAT. In TPPT, each I_3^- ion is situated in a local lattice pocket. The structures of TBAT and TPPT are derived from our x-ray data, and the depiction of TEAT is adapted from (*3*).

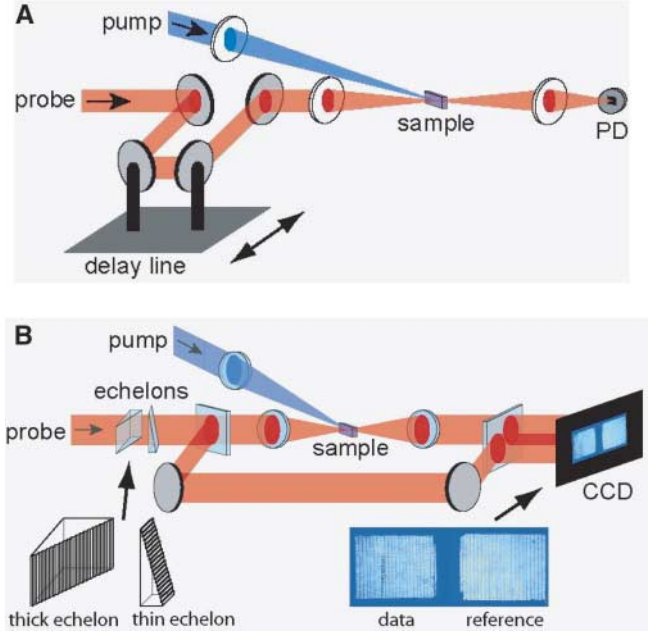

Fig. 2. Conventional and single-shot femtosecond spectroscopy. (**A**) In conventional femtosecond time-resolved measurements, an excitation (or pump) pulse initiates a reaction and a probe pulse monitors the evolution at a single, selected time delay *t* (PD, photodetector). The procedure is repeated for many different excitation-probe delays to provide a complete time-dependent data set. (**B**) In the present study, a complete data set is recorded following a single pump laser shot with 400 probe pulses that arrive at the sample successively delayed by 25-fs time increments and covering a total temporal range of 10 ps. The 400 pulses are formed from one original probe beam that is expanded in diameter and passed through two orthogonally oriented stair-step echelon structures. Portions of the probe pulse that pass through thicker combined glass regions are delayed by longer times. Each echelon has 20 steps, with step heights yielding relative delays of 25 fs in one structure and 500 fs in the other. The resulting 20 × 20 array of pulses is focused to a common spot at the sample position and then imaged onto a CCD camera, along with a reference image that bypasses the sample. The reference image is used to correct for variation in the incident beam spatial profile, imperfections in the echelon structures, and scattering of probe light due to imperfect sample optical quality. The CCD image shows data and reference images recorded from a single-shot measurement on a glass (fused silica) test sample. One vertical region of the data image shows substantial changes in probe pulse transmission through the sample, which are induced by the arrival of the excitation pulse. These changes last for ~300 fs (~12 distinct probe regions on the CCD image). The photoinduced responses of chemical interest in the present work are far smaller in magnitude and cannot be discerned by eye from the raw data images. The overall time resolution of the single-shot experimental setup, which is limited by probe pulse broadening within the echelons, the noncollinear pump-probe angles, and the optical properties of the samples, is ~50 fs.

approach is far more practical on femtosecond time scales, which require echelon step heights on the order of micrometers rather than millimeters. The advent of two-dimensional (2D) detector arrays and sophisticated computer-based image-processing techniques has enabled the use of two echelons rather than one, thereby greatly increasing the number of time-delay sampling points that can be recorded in a single laser shot (*21*–*23*). Our initial demonstrations of this approach focused on catastrophic sample damage under extreme high-intensity irradiation (*21*, *22*) and, more recently, on reaction dynamics in supercooled liquids and amorphous solids with essentially perfect optical quality and uniformity (*23*). In the present work, through substantial improvements in sensitivity and automated data analysis, we are able to extend single-shot methods to the study of chemical reaction dynamics in homegrown organic crystals. In such samples, the scattered probe light intensity typically exceeded the induced change in probe transmission that was being measured, and the pattern of scattered light at the charge-coupled device (CCD) detector changed appreciably from one crystalline region to another. The entire 20 × 20 grid pattern of transmitted probe beams at the CCD, as well as distortions of the grid pattern, also shifted as a sample crystal was translated because the front and back crystal faces through which the beams passed were not perfectly flat and parallel. To deal with these factors, we developed advanced algorithms in our laboratory for pattern recognition of the 20 × 20 data and reference array grids superimposed over raw images; exclusion of CCD pixels at or near known irregularities (such as grid boundaries); scaled averaging over the roughly 1000 CCD pixels within each grid region that corresponds to a specific delay time; and normalization based on comparison between data and reference grids recorded first without, and then with, the excitation pulse. These measures, taken to improve the sensitivity of the experimental method, reduce the single-shot noise floor to ~0.1% of the transmitted probe light intensity (roughly two orders of magnitude lower than achievable otherwise), thereby enabling single-shot measurements of ultrafast photochemistry in organic crystals.

Transient absorption traces of the aforementioned crystals, each measured in a single laser shot, were acquired at seven probe wavelengths (three of which are shown in Fig. 3) spanning the ground-state I_2^- absorption spectrum (*9*). Each laser shot impinged on a fresh region of the crystal. TPPT, the crystal with the least constrained environment around I_3^-, shows features that are typical of liquid-state triiodide photochemistry (*12*): initial absorption at all probe wavelengths from the I_3^- excited state; formation, after ~400 fs, of I_2^- and I photofragments as evidenced by the characteristic I_2^- absorption spectrum centered near 740 nm; coherent vibrational oscillations of the I_2^- fragment, which by alternately stretching and compressing gives rise to corresponding blue- and red-shifting of its absorption spectrum (fig. S1); and vibrational dephasing and cooling, the former marked by the decay of the coherent oscillations and the latter by a gradual narrowing of the absorption spectrum (observed as substantial decay of absorption at the wings and slower decay or rise of absorption at the center of the spectrum) as the initially excited vibrational population relaxes to the bottom of the I_2^- potential well.

Similar behavior is observed within the first picosecond in the two crystals with more severely constrained environments around the anions: I_3^- excited-state absorption and fragmentation followed by coherent vibrational oscillations of the I_2^- photoproduct. At later times, however, the dynamics differ strikingly from those observed in TPPT or in liquid-state environments. In TBAT, which confines the I_3^- ions within pseudo-columnar channels formed by the tetrabutylammonium counterions, I_2^- absorption decays abruptly and almost completely after 1.1 to 1.3 ps. In the intermediately constrained environment of TEAT, the I_2^- absorption decays 1.4 to 1.7 ps after the initial photolysis, somewhat later and less abruptly than in TBAT. These results suggest substantial lattice environmental effects on the chemistry of the nascent photofragments.

The reaction dynamics were explored further through molecular dynamics simulations. Model systems of 3 × 3 × 3 unit cells were constructed using reported potentials for I_3^- and I_2^- (*14*, *24*, *25*), bond-order potentials (*26*, *27*) for certain covalently bonded counterions, and Lennard-Jones potentials for interactions between other bonded and nonbonded atoms (*9*). A Gaussian thermal distribution of 30,000 trajectories at 298 K was constructed and propagated forward in time in each simulation. Simulations were launched in each model crystal by placing each of the reactive I_3^- ions in a selected electronic excited state (*9*) and then solving the classical equations of motion for each atom; the well-established Verlet algorithm was used to compute new atomic positions and momenta after successive 1-fs time increments. We focus on calculation of I_2^- absorption because this is the experimentally measured property that reveals the lattice-mediated dynamics of key interest. Formation of I_2^- is initiated by defining a "dissociation distance" for the parent I_3^- ion. The first of the two terminal I atoms to move beyond the dissociation distance from the central atom is considered to have dissociated, and the other two I atoms, which remain bonded, are smoothly transferred to the ground-state I_2^- potential-energy surface. The dissociation distance is taken as roughly 115% of the mean equilibrium I_3^- bond length in order to reproduce the temporal onset of I_2^- absorption observed experimentally.

For all three crystals, the simulations reproduce semiquantitatively the onset of I_2^- absorption and coherent vibration. Crucially, the abrupt decay of I_2^- absorption in TBAT and TEAT and the absence of any such decay in TPPT are also reproduced. Individual trajectories selected at random out of the sets of 30,000 show highly consistent outcomes with the respective average trajectories (Fig. 4). The results support the conclusion that the abrupt disappearance of I_2^- spectral signatures arises from lattice reaction cage-mediated recombination of photofragments. In TBAT, the recombination is highly synchronized across the ~10^{12} excited unit cells and confined to a narrow time window of ~200 fs. In TEAT, the recombination is quite well synchronized, occurring mostly within a time window of ~300 fs. In TPPT, however, no signature of synchronized recombination is apparent in either experiment or simulation. In all three crystals, simulations show that the I_2^- fragment moves relatively little after I_3^- photodissociation, whereas the I fragment leaves with about 0.5 eV of kinetic energy, travels a substantial distance (3.3, 4.9, and 3.9 A on average, respectively, in

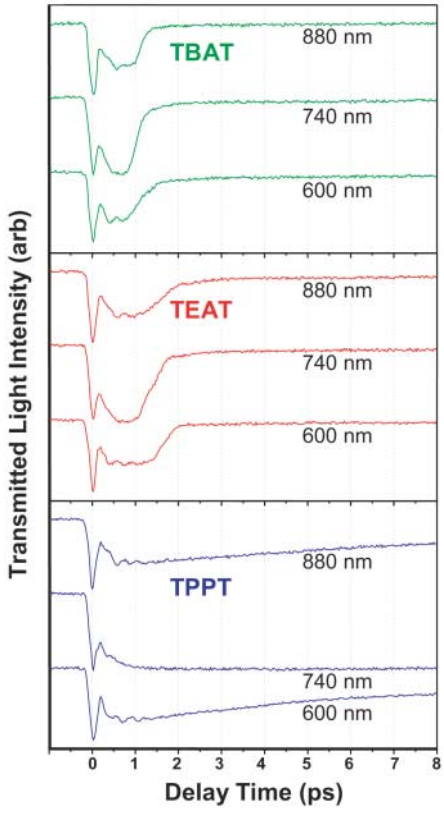

Fig. 3. Single-shot measurements of crystalline chemical reactions. Single-shot data from each of three different crystals are shown at three probe wavelengths. The maximum change in transmitted light intensity is ~2%.

TBAT, TEAT, and TPPT) before its first collision with a neighboring lattice constituent, and loses only a modest amount of its kinetic energy (4, 13, and 13%, respectively) during that encounter. In the TBAT lattice, the dissociated I atom moves away from its parent fragment, remaining within the confines of its pseudo-1D channel, until it collides with a neighboring I_2^- fragment. It then recoils principally along its original path of motion to recombine with its original partner. Although we have conducted classical numerical simulations of the motion, the simulation and experimental results and the particular lattice geometry of TBAT suggest approximate modeling, classically or quantum mechanically, in terms of a particle in a 1D box with rather little dephasing on the time scale of the single round trip that occurs before recombination. Thus, the photofragment's constrained translational motion, from inception through collision to recombination, is substantially phase-coherent. The dynamics are distinct from those observed in photolysis of I_2 in rare gas cryogenic matrices (*8*, *28*), in which energetic molecular states that are dissociative in the gas phase become "cage-bound" by lattice constraints that strongly resist even the initial dissociation event, so there is no free I translation before recoil, which occurs in the molecular electronic excited state but not the ground state. In the present case, a fully dissociated I atom undergoes a rather leisurely excursion whose distance is long compared to the original bond length (2.9 A) and whose duration is long compared to the period during which sudden recombination occurs. In the case of TEAT, this excursion lasts even longer and covers a longer distance. In TEAT, columns of I_3^- ions are oriented in roughly side-on stacks, so that the nearest-neighbor lattice environment for a dissociating I_3^- ion is formed mainly by pseudo-spherical tetraethylammonium ions and adjacent side-oriented I_3^- ions. Our simulations show that different initial conditions among the thermal distribution of I_3^- ions before photoexcitation, particularly different symmetric versus antisymmetric stretching and librational motions, produce different molecular trajectories that give rise to substantial variations in the interactions between a dissociated I atom and its neighbors. This results in recombination that is somewhat less synchronized than in TBAT, in which the local geometry is sufficiently restrictive that similar variations in initial conditions do not appreciably affect the recombination dynamics. Nevertheless, the degree of phase coherence in the recombination of TEAT as well as TBAT, apparent directly from the experimental data as well as from the simulations, is surprising given the complexity of organic crystalline environments generally. The TPPT crystal, whose local lattice surroundings present greatly reduced steric constraints as compared to TBAT and TEAT, permits a wide range of dissociated I-atom trajectories, and both experiment and simulation show no notable recombination during the time window following dissociation.

The experimental and computational results point consistently to a clear correlation between crystalline structure and reaction dynamics. In the cases examined here, well-defined variations in static structure lead to distinct recombination behavior on the part of caged photofragments. Dynamical effects involving transfer of photoproduct translational energy to lattice degrees of freedom, which may permit lattice accommodation of the permanent photoproducts that evidently are formed to some degree in all three crystals, should be studied as a function of temperature. In some systems, dense crystal packing around the reactive species and rapid flow of energy from molecular reactive modes into lattice modes may suppress even the initial photodissociative events. In partially disordered lattices, energy flow from the reactive mode into well-defined degrees of freedom [such as molecular rotation in plastic crystalline phases (*29*)] may suppress reaction through dissipation. This process should be more amenable to incisive analysis than is possible in liquids, which obscure similar phenomena on account of the wide range of ill-defined bath coordinates whose effects generally cannot be examined separately.

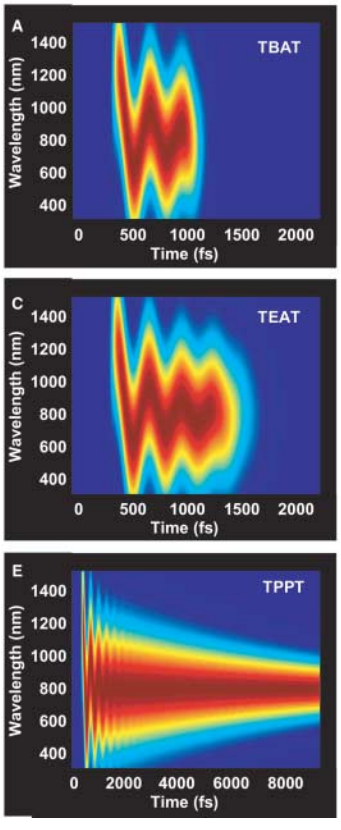

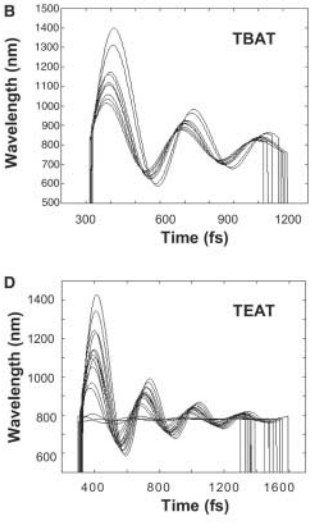

Fig. 4. Molecular dynamics simulations of crystalline chemical reactions. The results are averaged over 30,000 trajectories (left) and for randomly selected individual trajectories (right) for a model of I_3^- photolysis in 3 × 3 × 3 unit cells in (**A** and **B**) TBAT, (**C** and **D**) TEAT, and (**E**) TPPT. The abrupt end of I_2^- absorption in TBAT and TEAT is due to recombination of I_2^- ions with their original I atom partners to regenerate I_3^-. The trajectories shown in (A) and (B) illustrate that recombination is highly synchronized in TBAT and slightly less so in TEAT.

References and Notes

1. G. M. Schmidt, *J. Pure Appl. Chem.* **27**, 647 (1971).
2. J. R. Scheffer, C. Scott, *Science* **291**, 1712 (2001).
3. F. Toda, Ed., *Organic Solid State Reactions* (Springer, Berlin, 2002).
4. L. R. Ryzhkov, J. M. McBride, *J. Phys. Chem.* **100**, 163 (1996).
5. H. E. Zimmerman, E. E. Nesterov, *Acc. Chem. Res.* **35**, 77 (2002).
6. N. J. Turro, *Chem. Commun.* **124**, 2279 (2002).
7. G. R. Fleming, *Chemical Applications of Ultrafast Spectroscopy* (Oxford, New York, 1986).
8. R. Zadoyan, Z. Li, C. C. Martens, V. A. Apkarian, *J. Chem. Phys.* **101**, 6648 (1994).
9. Materials and methods are available as supporting material on *Science* Online.
10. J. R. Ferraro *et al.*, *J. Phys. Chem. Solids* **47**, 301 (1986).
11. T. Migchelsen, A. Vos, *Acta Crystallogr.* **23**, 796 (1967).
12. U. Banin, S. Ruhman, *J. Chem. Phys.* **99**, 9318 (1993).
13. E. Gershgoren, U. Banin, S. Ruhman, *J. Phys. Chem. A* **102**, 9 (1998).
14. T. Kühne, P. Vöhringer, *J. Chem. Phys.* **105**, 10788 (1996).
15. S. Hess, H. Bürsing, P. Vöhringer, *J. Chem. Phys.* **111**, 5461 (1999).
16. D. A. V. Kliner, J. C. Alfano, P. F. Barbara, *J. Chem. Phys.* **98**, 5375 (1993).
17. A. E. Johnson, N. E. Levinger, P. F. Barbara, *J. Phys. Chem.* **96**, 7841 (1992).
18. Z. Wang *et al.*, *Chem. Phys. Lett.* **313**, 155 (1999).
19. E. Gershgoren, J. Vala, R. Kosloff, S. Ruhman, *J. Phys. Chem.* **105**, 5081 (2001).
20. M. R. Topp, P. M. Rentzepis, R. P. Jones, *Chem. Phys. Lett.* **9**, 1 (1971).
21. G. P. Wakeham, K. A. Nelson, *Opt. Lett.* **25**, 505 (2000).

22. G. P. Wakeham, D. D. Chung, K. A. Nelson, *Thermochim. Acta* **384**, 7 (2002).
23. P. R. Poulin, K. A. Nelson, in *Ultrafast Phenomena XIV*, T. Kobayashi, T. Okada, T. Kobayashi, K. A. Nelson, S. De Silvestri, Eds. (Springer-Verlag, Berlin, 2005), pp. 529–531.
24. I. Benjamin, U. Banin, S. Ruhman, *J. Chem. Phys.* **98**, 8337 (1993).
25. E. C. M. Chen, W. E. Wentworth, *J. Phys. Chem.* **89**, 4099 (1985).
26. D. W. Brenner, *Phys. Rev. B* **42**, 9458 (1990).
27. D. W. Brenner *et al.*, *J. Phys. Condens. Matter* **14**, 783 (2002).
28. Z. Bihary, M. Karavitis, V. A. Apkarian, *J. Chem. Phys.* **120**, 7576 (2004).
29. J. N. Sherwood, Ed., *The Plastically Crystalline State (Orientationally-Disordered Crystals)* (Wiley, New York, 1978).
30. We thank P. Mueller for assistance in recording x-ray diffraction spectra. This work was supported in part by grants from the Office of Naval Research (N00014-01-1-0802 and N00014-06-1-0459).

Supporting Online Material
www.sciencemag.org/cgi/content/full/1127826/DC1
Materials and Methods
Fig. S1
References

23 March 2006; accepted 17 August 2006
Published online 31 August 2006;
10.1126/science.1127826
Include this information when citing this paper.

Anomalous Increase in Carbon Capacitance at Pore Sizes Less Than 1 Nanometer

J. Chmiola,[1] G. Yushin,[1] Y. Gogotsi,[1]* C. Portet,[2]† P. Simon,[2] P. L. Taberna[2]

Carbon supercapacitors, which are energy storage devices that use ion adsorption on the surface of highly porous materials to store charge, have numerous advantages over other power-source technologies, but could realize further gains if their electrodes were properly optimized. Studying the effect of the pore size on capacitance could potentially improve performance by maximizing the electrode surface area accessible to electrolyte ions, but until recently, no studies had addressed the lower size limit of accessible pores. Using carbide-derived carbon, we generated pores with average sizes from 0.6 to 2.25 nanometer and studied double-layer capacitance in an organic electrolyte. The results challenge the long-held axiom that pores smaller than the size of solvated electrolyte ions are incapable of contributing to charge storage.

Supercapacitors, also called electrical double-layer capacitors (EDLCs), occupy a region between batteries and dielectric capacitors on the Ragone plot describing the relation between energy and power (*1*). They have been touted as a solution to the mismatch between the fast growth in power required by devices and the inability of batteries to efficiently discharge at high rates (*2*, *3*). This large capacity for high power discharge is directly related to the absence of charge-transfer resistances that are characteristic of battery Faradaic reactions and subsequently leads to better performance at low temperature. Improvements in the energy density may accelerate the advent of electrical and fuel-cell cars, as well as enable numerous industrial and consumer applications for supercapacitors (*4*). Improvements have been made in cell packaging and electrolytes (*5*, *6*), but a lack of substantial progress in carbon material design has limited energy density, effectively preventing wide-scale usage of supercapacitors.

Unlike batteries and fuel cells that harvest energy stored in chemical bonds, supercapacitors exploit the electrostatic separation between electrolyte ions and high–surface area electrodes, typically carbon (*1*). This results in capacitances of tens of Farads per gram of active material, unlike traditional dielectric capacitors that have capacitances typically measured in microfarads. Energy stored in supercapacitors is linearly proportional to the capacitance of its electrodes, making material optimization crucial.

The large capacitance, C, and hence energy storage potential, of supercapacitors arises due to the small (~1 nm) separation, d, between electrolyte ions and carbon and high (typically 500 to 2000 m^2/g) specific surface area (SSA) of carbon electrodes according to

$$C = \frac{\varepsilon A}{d} \quad (1)$$

where A is the electrode surface area accessible to electrolyte ions, and ε is the electrolyte dielectric constant. Because SSA is explicitly related to pore size, understanding its effect on specific capacitance is especially important and has been the subject of numerous studies over the past decade (*7*–*9*).

Traditional methods of producing porous carbon from either natural precursors such as coconut shell or synthetic precursors such as phenolic resin do not offer sufficient control over porosity (*10*). Mesoporous carbons synthesized by template techniques have produced controllable pores in the range of 2 to 4 nm (*11*). It is believed that pores substantially larger than the size of the electrolyte ion and its solvation shell are required for high capacitance. The use of carbon nanotubes (*12*) has provided a good model system with large pores and high conductivity, leading to impressive power densities but low energy density.

A less well-known class of porous carbons offers great potential for controlling pore size. Carbide-derived carbons (CDCs) are produced by high-temperature chlorination of carbides, whereby metals and metalloids are removed as chlorides, leaving behind nanoporous carbon with a 50 to 80% open pore volume (*13*). Atomic-level porosity control in CDC is achieved by exploiting the host carbide lattice as a template, permitting controlled layer-by-layer metal extraction by optimizing the chlorination parameters. CDCs have a narrow pore-size distribution with a mean value that is tunable with better than 0.05-nm accuracy in the range of ~0.5 to ~3 nm (*14*) and a SSA up to 2000 m^2/g (*15*), which make them attractive candidates for studying porosity in supercapacitor applications. The ease of pore tunability in CDC previously allowed experimental determination of the optimal pore size for hydrogen storage (*16*). Also, CDC has shown impressive specific capacitance when used as the active material in supercapacitors with many electrolyte systems (*17*–*20*). The use of CDC allows precise control over properties found in all carbon materials, allowing broad trends to be discovered that are applicable to other carbons. Previous work with titanium carbide–derived carbon (TiC-CDC) as the active material in supercapacitors with aqueous H_2SO_4 electrolyte (*18*) showed a correlation between the micropore size (pores <2 nm) and capacitance but did not explore pores smaller than 1 nm. This study focused on the small-pore effect by using CDC with pores tuned from 0.6 to 2.25 nm and an electrolyte consisting of a 1.5 M solution of tetraethylammonium tetrafluoroborate in acetonitrile.

TiC-CDC was synthesized by chlorination at 500° to 1000°C (*21*), and its bulk properties were characterized by Raman spectroscopy and transmission electron microscopy (TEM). Conductivity measurements were performed on compacted powders. Porosity was characterized by argon sorption at 77 K and confirmed with data from small-angle x-ray scattering (SAXS) (*22*) and CO_2 sorption at 300 K. The use of multiple techniques for porosity measurement ensures greater confidence in the results. Elec-

[1]Department of Materials Science and Engineering and A. J. Drexel Nanotechnology Institute, Drexel University, Philadelphia, PA 19104, USA. [2]Université Paul Sabatier, CIRIMAT, UMR CNRS 5085, 31062 Toulouse Cedex 4, France.

*To whom correspondence should be addressed. E-mail: gogotsi@drexel.edu

†Present address: Department of Materials Science and Engineering, Drexel University, Philadelphia, PA 19104, USA.